Engineering Failure Analysis 166 (2024) 108908

Contents lists available at ScienceDirect

Engineering Failure Analysis

journal homepage: www.elsevier.com/locate/engfailanal

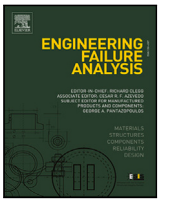

Prediction of fatigue life of a bolted joint in railway steel arch bridge using multiaxial fatigue criteria

Emanuele Maiorana [a], Angelo Aloisio [b,*], Valdinique Tasse [c,d], Bruno Briseghella [e]

[a] Department of Economics, Science, Engineering and Design, University of the Republic of San Marino, Via Consiglio dei Sessanta 99, 47891 Dogana, San Marino
[b] Department of Civil, Building-Architecture and Environmental Engineering, Università degli Studi dell'Aquila, L'Aquila, Italy
[c] Department of Civil Engineering, National Advanced School of Public Works of Yaoundé, Cameroon
[d] University of Padova, Via Marzolo 9, 35121 Padova, Italy
[e] College of Civil Engineering, Fuzhou University, Fuzhou, China

ARTICLE INFO

Keywords:
Fatigue life estimation
Railway bridge engineering
Multiaxial fatigue damage
Rainflow counting method

ABSTRACT

Fatigue represents a critical condition for infrastructure subjected to repeated cyclic loads, such as steel railway bridges. The literature offers several methods to estimate fatigue life, consisting of three main phases: cycle counting, fatigue damage criterion, and damage accumulation criterion. Applying S–N curves might not be conservative in the case of railway bridges subjected to traffic because the stress-time history is complex and cannot be reduced to a sinusoidal history. Additionally, the presence of a multiaxial stress state must be considered. Therefore, this work compares eight multiaxial fatigue damage criteria for evaluating fatigue life in a scenario between high and low-cycle fatigue. Specifically, the authors considered four low-cycle fatigue criteria, namely Smith–Watson–Topper (SWT), Kandil, Brown and Miller (KBM), Glinka, Fatemi and Socie (FS), and four high-cycle fatigue criteria, Crossland, Basquin and the methods recommended by Eurocode 3 and British Standard. The rainflow counting method in ASTM E1049-85 (2011) and Miner's rule for damage accumulation were used. The Polcevera railway steel bridge was selected as a case study. A 3D numerical model was developed for this purpose using Midas Civil software, taking into account the material non-linearity of the bridge's elements. Once the area with the highest stress concentration was identified, a detailed analysis was conducted to estimate the stress and strain time histories induced by train traffic. A sensitivity analysis was conducted after critically comparing the eight methods for predicting fatigue life to assess the impact of traffic parameters, train velocity, axle load, and convoy length on fatigue life. It has been found that the criteria considering axial stress tend to overestimate the number of fatigue cycles to failure compared to the criteria, including the effect of shear stress components.

1. Introduction

Over the past few decades, the behavior of infrastructures under an increasing number of heavier vehicles has raised significant concerns. This trend has intensified stresses, resonance issues, and excessive vibrations and accelerated the aging of materials. These challenges have prompted design professionals to re-evaluate the vulnerability and durability of bridges critically [1–5].

* Corresponding author.
E-mail address: angelo.aloisio1@univaq.it (A. Aloisio).

https://doi.org/10.1016/j.engfailanal.2024.108908
Received 12 August 2024; Received in revised form 19 September 2024; Accepted 21 September 2024
Available online 28 September 2024

Despite these pressing issues, current engineering design codes still fall short of including comprehensive guidelines that effectively integrate the effect of fatigue on bridge responses to traffic loads and non-linear behavior into bridge design practices [6].

In the case of steel railway bridges, fatigue is a particularly critical issue due to the presence of repeated cyclic loads of significant amplitude [7–10]. Fatigue damage in metals is associated with the nucleation and growth of microcracks, generally intercrystalline, under cyclic loading until the initiation of a macroscopic crack. This phenomenon can occur at lower stress levels than the conventional elastic limit [11]. It is possible to distinguish between fatigue with a large number of cycles, which involves elastic deformations and which corresponds to a high number of cycles to failure, and fatigue with a low number of cycles (or low-cycle fatigue) where plastic deformations occur [12]. The fatigue life assessment requires three main ingredients: (i) a cycle counting method, (ii) a damage criterion, (iii) and a damage accumulation model. The authors will present the main challenges of the three when applied to steel infrastructures.

(i) The complexity of the fatigue assessment in railway bridges also lies in managing the response under non-sinusoidal block loads, where the direct application of the S–N method is not possible. Additionally, using equivalent stress approaches to determine fatigue damage in block loading scenarios often leads to underestimated fatigue life predictions. Specifically, these approaches fail to account for the extent of fatigue damage within a loading block, typically resulting in non-conservative estimates. Therefore, a reliable cycle counting method is necessary. The use of rain flow cycle counting to analyze the time variation of equivalent stress often fails to accurately predict the complex fatigue damage behaviors in multiaxial scenarios [13,14]. There are currently few advancements in cycle counting methods [15–18]. However, given the lack of up-and-coming methods and the complexity of their implementation in professional practice [19], it is considered prudent to rely on established methods such as the ASTM E1049-85 (2011) standard [20]. This method can be applied separately for each stress and then appropriately combined based on the multiaxial fatigue criteria.

(ii) In the service life of infrastructures, multiaxial stresses are prevalent, where two or three principal stresses vary over time, often being out-of-phase or changing in direction during a load cycle. This complexity requires adopting multiaxial fatigue analysis to accurately estimate these components' fatigue strength. Factors influencing multiaxial stress include the type of loading, complex geometries of parts, and inherent residual or pre-stresses [21]. Therefore, as stress levels increase, classical methods based on uniaxial criteria, such as the Goodman method, are not applicable due to the presence, in the simplest cases, of both normal and shear stresses. Moreover, in the case of railway infrastructures, the literature lacks a critical comparison of the available fatigue damage criteria. There are three classes of multi-axial fatigue criteria:

- Stress-Based Criteria: Methods proposed by Susmel and Lazzarin [22], McDiarmid [23], and Crossland [24] focus primarily on stress and are most applicable to high-cycle fatigue scenarios where deformations remain largely elastic.
- Strain-Based Criteria: Models such as those by Brown–Miller [25], Fatemi–Socie [26], and Li–Zhang [27] are suited for conditions with notable plastic deformation.
- Energy-Based Criteria: These criteria incorporate both stress and strain components and are exemplified by models from Smith–Watson–Topper [28], Glinka et al. [29], and Varani–Farahani [30].

Additionally, multiaxial fatigue criteria can be differentiated by using the critical plane concept, which identifies a material plane where stress or strain components peak. This concept, initially introduced by Brown and Miller [25], focuses on maximizing the shear strain to predict fatigue life. Socie [31] extended this concept, introducing the Smith–Watson–Topper parameter to better predict tensile-type failures by emphasizing crack growth perpendicular to the maximum tensile stress. Moreover, the integration of energy criteria with the critical plane approach, as suggested by Liu [32] and Glinka et al. [29], alongside Varani–Farahani's [30] takes into account both axial and shear fatigue properties. Despite extensive research by Papadopoulos et al. [33], Sonsino [34], and others [35–41], the challenge of accurately predicting fatigue life under multiaxial loading remains, especially for civil structures.

(iii) Regarding the accumulation of damage, the majority of methods in the literature typically utilize Miner's Rule or its adaptations, which are conventionally applied in uniaxial scenarios [42]. Miner's Rule combines a specific damage parameter with a cycle counting technique, crucial for capturing the genuine fatigue behavior of materials [15,43–45].

This work aims to understand and compare literature methods for predicting the number of cycles to failure under multiaxial stress states in a scenario between high and low-cycle fatigue. While the bridge's response remains prevalently elastic, with increasing axle loads, the stress gets close to the yielding limit in some cases. Therefore, the authors selected four high- and four low-cycle criteria to thoroughly predict fatigue life. While substantial research exists in the automotive and aircraft industries, fewer studies address civil infrastructure. The primary reason is that stress levels are generally lower in civil structures. However, this is not always the case, and significant stress concentrations can occur, especially in bolted and welded joints commonly used in steel structures. The introduction of geometric discontinuities, such as those created by drilling holes for bolted joints, typically results in stress concentrations that significantly increase the potential for fatigue crack initiation and propagation under cyclic loading conditions [46–49]. Despite this, bolted joints are extensively utilized due to their assembly convenience and the feasibility of disassembly, which offer significant practical advantages [39,50–54].

Therefore, it is crucial to apply multiaxial fatigue criteria along with suitable cycle counting methods to civil infrastructures [46,55,56]. To the authors' knowledge, such methods have not been critically applied and compared in the context of civil infrastructures [57], while there is a substantial literature in another engineering fields. The authors have chosen a representative case study of a typical steel arch bridge, the Polcevera Bridge. On this bridge, they applied various methods for predicting fatigue life and evaluated the sensitivity of these predictions to traffic parameters, such as axle load, number, and velocity.

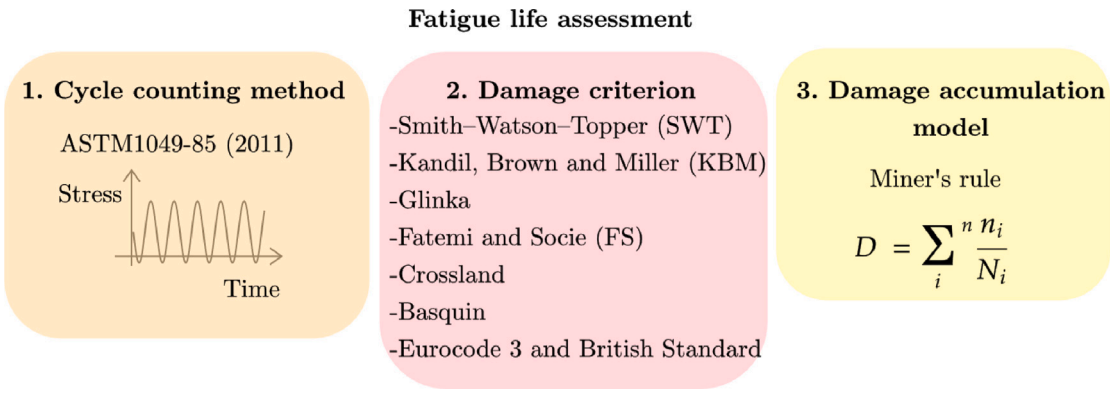

Fig. 1. Main steps of fatigue life assessment.

2. Theoretical background

Assessing block loading damage requires the integration of three principal fatigue methodologies: a cycle counting method, a damage criterion, and a damage accumulation model, as shown in Fig. 1.

2.1. Cycle counting: the rainflow cycle counting method

The rainflow cycle counting method is a technique used in fatigue analysis to determine the number and magnitude of stress or strain cycles experienced by a material under variable loading conditions. The method was developed by Tatsuo Endo and M. Matsuishi in 1968 [58] at the University of Kyoto. It was originally inspired by the way rain flows down a pagoda roof, with each successive ledge interrupting the flow and causing the "rainflow" to reverse, much like the reversal in stress–strain cycles in a material under cyclic loading. The method works by identifying cycles within a randomly varying stress–strain history. The method is based on identifying peaks and troughs in the stress/strain signal. The method classifies the amplitude and mean of stress or strain cycles from the turning points. The method counts half-cycles and full-cycles. A full cycle occurs when the load sequence returns to the start load level, completing a loop. The authors implemented the rainflow counting method defined in the ASTM E1049-85 (2011) standard [20]. It uses the three-point method for cycle counting. A cycle is identified when three consecutive points can be rearranged to form a hysteresis loop without encompassing any point outside this trio. The ASTM E1049-85 method is widely used in automotive and aerospace, with limited application in civil infrastructures [19]. The authors provided the following pseudocode of the ASTM E1049-85 method, implemented in Matlab.

Algorithm 1 ASTM Rainflow Counting Method

Initialize stress sequence S
Initialize cycle count array C
Define the total number of stress reversals R
Calculate stress reversals from S
Initialize index $i \leftarrow 1$
while $i \leq R - 2$ **do**
    Calculate stress range $X \leftarrow |S[R(i+1)] - S[R(i)]|$
    Calculate stress range $Y \leftarrow |S[R(i+2)] - S[R(i+1)]|$
    Calculate mean stress $M \leftarrow (S[R(i+1)] + S[R(i)])/2$
    if $X < Y$ **then**
        Add half cycle (X, M) to C
        $i \leftarrow i + 1$
    else
        Add full cycle (Y, M) to C
        $i \leftarrow i + 2$
    end if
end while
Output cycle counts and ranges for fatigue analysis

For multiaxial loading, the rain flow method is applied separately to the axial and shear stress components, following the approach described in the ASTM E1049-85 (2011) standard [20].

2.2. Fatigue criteria

The authors expect that the bridge response, despite being in the elastic range, might fall between high and low-cycle fatigue when, under high axle load, the stress approximates the yielding limit. Therefore, they compared four low-cycle fatigue criteria (Smith–Watson–Topper (SWT), Kandil, Brown and Miller (KBM), Glinka, Fatemi and Socie (FS)) and four high-cycle fatigue criteria (Crossland, Basquin, Eurocode 3 and British Standard) to estimate the fatigue life of a railway steel bridge under traffic load.

The SWT introduces a critical plane approach that focuses on the maximum normal stress on the critical plane, while KBM extends the SWT to include the shear stresses. Glinka employs an energy-based method to relate stress and strain components to fatigue life. FS is another critical plane approach that focuses on shear strains and stresses. Crossland estimates fatigue using a combination of maximum principal stress and octahedral shear stress. Basquin is a very old approach based on an empirical relationship between stress amplitude and the number of cycles to failure, which has become widely used for high-cycle fatigue analysis. The methods recommended by Eurocode 3 and the British Standard are based on the classical S–N curve approach.

2.2.1. Smith–Watson–Topper (SWT)

The Smith–Watson–Topper (SWT) method can be expressed as follows for predicting the fatigue life under cyclic loading conditions [59]:

$$\frac{\sigma_n^{\max}\Delta\epsilon_1}{2} = \left(\frac{\sigma_f'^2}{E}\right)(2N_f)^{2b} + \sigma_f'\epsilon_f'(2N_f)^{b+c} \tag{1}$$

In this expression, $\sigma_n^{\max}$ represents the peak normal stress, and $\Delta\epsilon_1$ denotes the maximum range of the first principal strain, both evaluated at the most critical plane of the structure. The highest product value of these parameters is used to calculate the fatigue life, derived from cyclic stress analysis at various points in finite element models. For structural steel, the constants used for fatigue calculations are, $E = 210$ GPa; Fatigue strength coefficient, $\sigma_f' = 1170$ MPa; Fatigue ductility coefficient, $\epsilon_f' = 0.12$; Fatigue strength exponent, $b = -0.087$; Fatigue ductility exponent, $c = -0.53$ [60].

2.2.2. Kandil, Brown and Miller (KBM)

The Kandil, Brown and Miller (KBM) multiaxial theory offers a physical interpretation of fatigue crack growth mechanisms [61, 62]. The fatigue assessment is based on the following equation:

$$\frac{\Delta\gamma_{\max}}{2} + S_k\Delta\epsilon_n = \frac{\sigma_f'}{E}(2N_f)^b + \epsilon_f'(2N_f)^c \tag{2}$$

where $\Delta\gamma_{\max}$ is the maximum shear strain range observed, $\Delta\epsilon_n$ represents the normal strain range on the critical plane, indicative of maximum shear strain, S_k is a material-dependent constant optimized for matching fatigue life predictions with empirical uniaxial stress test results. The constant S_k for steel is typically set to 0.9 based on experimental calibration [60]. The critical plane for this analysis is where the shear and normal strains due to cyclic loads reach their maximum values.

To compute the normal strain range, $\Delta\epsilon_n$, the following equations are used:

$$\Delta\epsilon_n = \left(\frac{\epsilon_1 - \epsilon_3}{2}\right)_{\theta_1} - \left(\frac{\epsilon_1 - \epsilon_3}{2}\right)_{\theta_2} \tag{3}$$

$$\Delta\epsilon_n = \left(\frac{\epsilon_1 + \epsilon_3}{2}\right)_{\theta_1} - \left(\frac{\epsilon_1 + \epsilon_3}{2}\right)_{\theta_2} \tag{4}$$

Here, θ_1 and θ_2 represent phases of loading and unloading within the fatigue cycle, respectively.

2.2.3. Glinka

Glinka et al. [29] introduced a fatigue parameter that involves the summation of both elastic and plastic energy densities evaluated on the critical shear plane. The following formula is utilized to assess fatigue damage by integrating stress and strain measures:

$$\frac{\Delta\gamma}{2}\frac{\Delta\tau}{2} + \frac{\Delta\sigma_n}{2}\frac{\Delta\epsilon_n}{2} = \frac{\sigma_f'^2}{2E}(2N_f)^{2b} + \frac{E\epsilon_f'}{2}(2N_f)^{b+c} \tag{5}$$

$\Delta\gamma$ and $\Delta\tau$ denote the shear strain range and the shear stress range, respectively, while $\Delta\epsilon_n$ and $\Delta\sigma_n$ represents the normal strain and stress ranges on the critical plane. These metrics can be extracted from the results of finite element analysis, specifically examining the principal stresses and strains.

The following equations define the process to compute $\Delta\tau$ and $\Delta\sigma_n$ from principal stress differences:

$$\Delta\tau = (\sigma_1 - \sigma_3)_{\theta_1} - (\sigma_1 - \sigma_3)_{\theta_2} \tag{6}$$

$$\Delta\sigma_n = \left(\frac{\sigma_1 + \sigma_3}{2}\right)_{\theta_1} - \left(\frac{\sigma_1 + \sigma_3}{2}\right)_{\theta_2} \tag{7}$$

In these equations, σ_1 and σ_3 are the highest and lowest principal stresses, respectively, with θ_1 and θ_2 marking the loading and unloading phases of the stress cycle.

2.2.4. Fatemi and Socie (FS) criterion

The Fatemi–Socie criterion [63], which is strain-based, considers the plane of maximum shear strain amplitude as the critical plane. This approach is summarized in the following expression:

$$\frac{\Delta\gamma_{\max}}{2}\left(1+k\frac{\sigma_{n,\max}}{\sigma_y}\right)=\frac{\tau'_f}{2G}(2N_f)^b+\gamma'_f(2N_f)^c \tag{8}$$

where $\Delta\gamma_{\max}$ is the peak shear strain experienced on the critical plane; $\sigma_{n,\max}$ represents the maximum normal stress on the same plane; $k=0.3$ is the Fatemi–Socie constant; σ_y is the tensile yield strength; τ'_f, γ'_f, and G are the torsional fatigue strength, ductility coefficients, and shear modulus, respectively; b' and c' are the exponents for fatigue strength and ductility defined in the previous subsections.

2.2.5. Crossland's criterion

Crossland's method [24] uses the second invariant of the deviatoric stress tensor combined with the maximum hydrostatic stress:

$$\sqrt{J_{2a}}+k\cdot\sigma_{H,\max}=\sigma'_f\cdot(2N_f)^b \tag{9}$$

This criterion can be expressed through the second invariant of deviatoric stress tensor J_{2a} calculated as:

$$\sqrt{J_{2a}}=\frac{1}{2\sqrt{6}}\left[(\Delta\sigma_1-\Delta\sigma_2)^2+(\Delta\sigma_2-\Delta\sigma_3)^2+(\Delta\sigma_1-\Delta\sigma_3)^2\right]^{1/2} \tag{10}$$

$\Delta\sigma_i$ represents the range of principal stresses; $\sigma_{H,\max}$ is the peak hydrostatic stress; k is a material constant, typically set to unity.

Crossland is more suitable for multiaxial stress states, such as in complex structures where different stress components (shear and normal) act simultaneously, such as in aerospace, automotive, or civil structures. Material Behavior: It considers the combined effects of shear and normal stresses, making it more versatile for multiaxial loading situations.

2.3. Basquin's law

Basquin [64,65] introduced the empirical relationship between stress amplitude and the number of cycles to failure, which has become widely used for high-cycle fatigue analysis. Basquin's law is one of the foundational models in studying fatigue behavior in materials, especially metals like steel. The Basquin's law is given by [65]

$$S=\sigma'_f(2N)^b \tag{11}$$

where S is the stress amplitude (or alternating stress), N is the number of cycles to failure, σ'_f is the fatigue strength coefficient, and b is the fatigue strength exponent, whose values are given in the former subsections.

2.4. Eurocode 3

According to the Eurocode 3 [66], the fatigue strength for nominal stress ranges is represented by a series of S–N curves, where the number of cycles to failure N is related to both the axial stress range $\Delta\sigma_R$ and the shear stress range $\Delta\tau_R$. These S–N curves are defined in logarithmic form. For the axial stress component, the fatigue strength can be calculated using the following equations:

$$\Delta\sigma_R^m N=\Delta\sigma_C^m\cdot 2\times10^6,\quad \text{with } m=3 \text{ for } N\le 5\times10^6 \tag{12}$$

$$\Delta\sigma_R^m N=\Delta\sigma_D^m\cdot 5\times10^6,\quad \text{with } m=5 \text{ for } 5\times10^6\le N\le 10^8 \tag{13}$$

where N is the predicted number of cycles to failure for a stress range $\Delta\sigma_R$, $\Delta\sigma_C$ is the reference value of the axial stress range for 2 million cycles, $\Delta\sigma_D=0.737\Delta\sigma_C$ is the constant amplitude fatigue limit for axial stress. For the shear stress component, the fatigue life is similarly calculated using the following equations:

$$\Delta\tau_R^m N=\Delta\tau_C^m\cdot 2\times10^6,\quad \text{with } m=3 \text{ for } N\le 5\times10^6 \tag{14}$$

$$\Delta\tau_R^m N=\Delta\tau_D^m\cdot 5\times10^6,\quad \text{with } m=5 \text{ for } 5\times10^6\le N\le 10^8 \tag{15}$$

where N is the predicted number of cycles to failure for a shear stress range $\Delta\tau_R$, $\Delta\tau_C$ is the reference value of the shear stress range for 2 million cycles, $\Delta\tau_D=0.737\Delta\tau_C$ is the constant amplitude fatigue limit for shear stress.

The fatigue damage is considered negligible if the stress range is below the cut-off limit. The cut-off limit is given by:

$$\Delta\sigma_L=\left(\frac{2}{100}\right)^{1/5}\Delta\sigma_C=0.457\Delta\sigma_C \tag{16}$$

$$\Delta\tau_L=\left(\frac{2}{100}\right)^{1/5}\Delta\tau_C=0.457\Delta\tau_C \tag{17}$$

These limits represent the lowest stress ranges for which fatigue is still considered.

Table 1
Mean-line S-N relationships (BS 5400).

Detail class	K_0	Δ	m
W	0.37×10^{12}	0.654	3.0
G	0.57×10^{12}	0.662	3.0
F2	1.23×10^{12}	0.592	3.0
F	1.73×10^{12}	0.605	3.0
E	3.29×10^{12}	0.561	3.0
D	3.99×10^{12}	0.617	3.0
C	1.08×10^{14}	0.625	3.5
B	2.34×10^{15}	0.657	4.0
S	2.13×10^{23}	0.313	8.0

Table 2
Probability factors (BS 5400).

Probability of failure	d
50%	0.0
31%	0.5
16%	1.0
2.3%	2.0
0.14%	3.0

2.5. British standard

The $S--N$ curves provided in the British Standard, BS 5400 [67], were formulated through statistical analyses of available experimental data (linear regression analysis of log S and log N) with minor empirical adjustments to ensure compatibility between various categories. The following equation represents the S–N relationship:

$$N \cdot S^m = K_0 \cdot \Delta^d \tag{18}$$

where N is the predicted number of cycles to failure for a stress range S, m is the inverse slope of the mean-line log S-log N curve, K_0 is a constant related to the mean-line log S-log N curve, Δ is the reciprocal of the anti-log of the standard deviation of log N, d is the number of standard deviations below the mean-line log S-log N curve, also called the probability factor, and different values of d correspond to varying probabilities of failure.

It should be remarked that, to handle low-stress ranges, the BS 5400 recommends reducing the number of repetitions of each stress range to less than the fatigue limit, S_0, by multiplying a reducing factor, λ_i, which is defined as:

$$\lambda_i = \begin{cases} \left(\frac{S_i}{S_0}\right)^2, & \text{if } S_i < S_0 \\ 1, & \text{if } S_i \geq S_0 \end{cases} \tag{19}$$

where S_i is the stress range of the cycle, S_0 is the fatigue limit (below which the fatigue damage is negligible), λ_i is the reducing factor. The parameters of Eq. (22) are given in Tables 1 and 2.

The authors adopted the values for class B and a probability of failure of 2.3%, which is also considered the reference value.

2.6. Damage accumulation criterion and fatigue life assessment

Miner's Rule [42] is used to calculate the cumulative damage in a material under cyclic loading.

$$D = \sum_{i=1}^{n} \frac{n_i}{N_i} \tag{20}$$

where n_i is the number of cycles at stress amplitude σ'_{ai}, N_i is the number of cycles to failure at the adjusted stress amplitude from the S–N curve. The material is considered to have failed when $D \geq 1$. To estimate the fatigue life in years, consider the annual damage calculated using Miner's Rule based on traffic load data:

$$T = \frac{1}{D_{annual}} \tag{21}$$

where D_{annual} is the cumulative damage per year. The resulting T represents the estimated number of years before failure. The authors also considered the approach by Bannantine and Socie, who proposed a multiaxial cumulative damage criterion based on a mix of critical plane damage parameters, rain flow cycle counting methods and Miner's rule. The main idea is to get the total fatigue damage through a combination of two different damage behaviors. Eq. (22) expresses this concept, where the largest fatigue damage occurs in the plane with the smallest value of $N(\theta)$ (i.e. the critical plane).

$$\frac{1}{N(\theta)} = \frac{1}{N_\sigma(\theta)} + \frac{1}{N_\tau(\theta)} \tag{22}$$

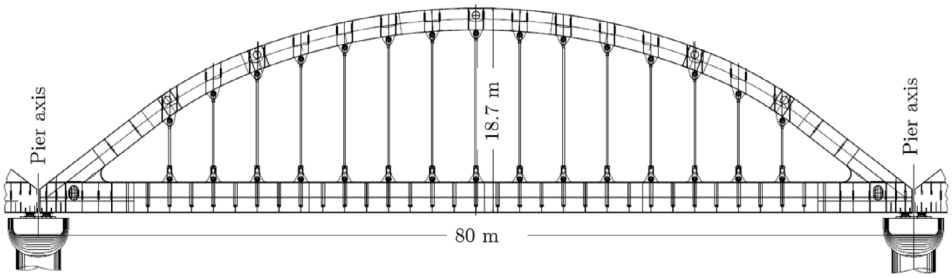

(a)

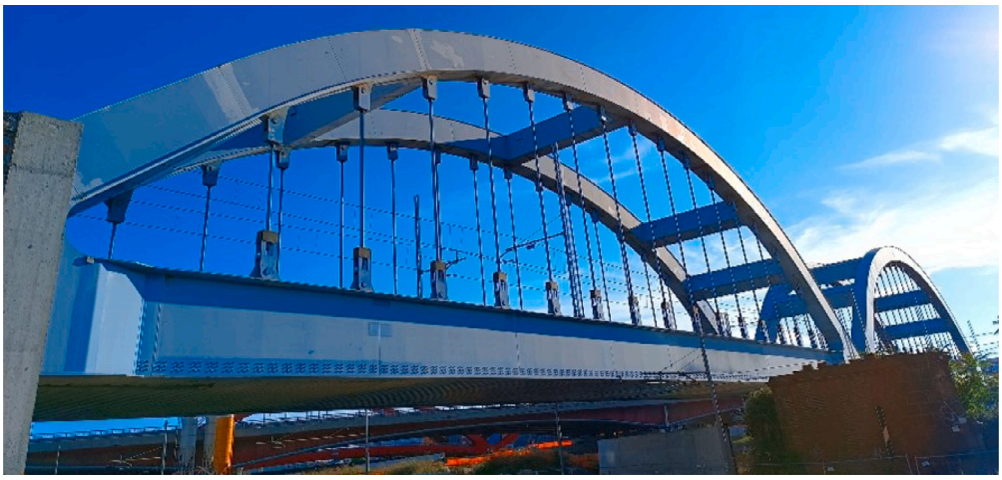

(b)

Fig. 2. (a) Technical drawing and (b) view of the bridge.

$N_\sigma(h)$ and $N_\tau(h)$ are the fatigue life estimations obtained through a critical plane based on axial and shear strains, respectively.

3. Case study: the Polcevera bridge

3.1. Bridge description

The bridge is located in the Sampierdarena area of Genoa, specifically within the former ILVA Cornigliano site. It crosses the Polcevera stream, see Fig. 2.

It is a steel arch bridge with a total length of 179.5 m, primarily composed of two identical arches each spanning 80 m. The structural typology utilized for these 80-meter spans, features an eliminated thrust arch at the base and braced walls at the top.

The length of each beam, measured between the axes of the supports, is 80 m, while the distance between the walls (the width of the bridge) is 10.80 m. Each wall connects to the main beam through 15 hangers with a 4-meter pitch, comprised of round bars made from special S460 NL steel with a nominal diameter of Φ 130 mm. The arch-to-deck connection is facilitated by a special end segment (referred to as a "shoe"), which connects the arch cores to the core of the beam-chain.

The arch is constructed with a caisson Section 2 meters high, featuring an upper flange of 1500 × 35 mm, a lower flange of 1500 × 35 mm, and two cores of 30 mm each; the height at the arch's crown is 18.70 m. The beams are constructed with a double T-section, 2.80 meters in height, with an upper flange of 1000 × 40 mm, a lower flange of 1000 × 40 mm, and a core thickness that increases from 20 mm to 40 mm at the joint with the arch.

The remaining span consists of a simply supported deck with a length of 10.80 meters between the support axes. The beams have a double T-section (resembling an I-section) of 2.80 meters in height, with an upper flange of 1000 × 30 mm (segment 1) and 1000 × 35 mm (segment 2), a lower plate of 1000 × 30 mm (segment 1) and 1000 × 35 mm (segment 2), and cores of 20 mm (segment 1) and 18 mm (segment 2). The support surface for the railway infrastructure consists of a deck with HEB 600 steel beams embedded in a concrete slab of at least 650 mm thickness; the slab's extrados has a waterproofing mantle with an overlying protective screed. The retaining walls of the ballast and the slab are equipped with Φ 130 mm holes for water drainage.

More details on the bridge construction can be found in [68].

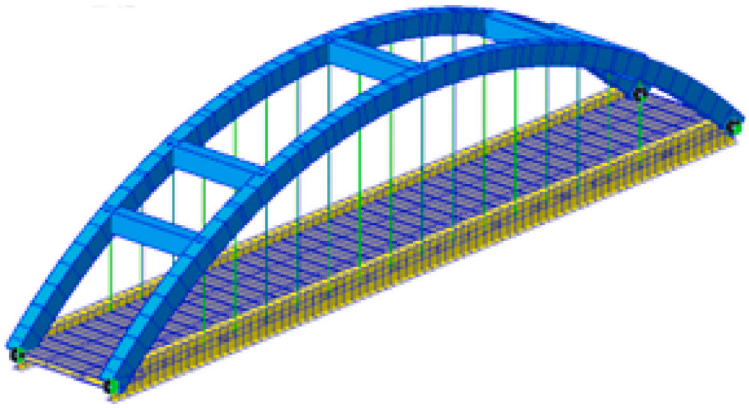

Fig. 3. Numerical model of the bridge in Midas.

Table 3
Characteristics of the structural steel used (S 420).

Property	Unit	Value
Characteristic ultimate strength	MPa	520
Characteristic yield strength	MPa	420
Elastic modulus	MPa	210,000
Ultimate limit state safety factor		1.05
Design yield strength	MPa	400

Table 4
Mechanical characteristics of steel used for hangers (S 460 N/NL).

Property	Unit	Value
Characteristic ultimate strength	MPa	540
Characteristic yield strength	MPa	460
Elastic modulus	MPa	210,000
Ultimate limit state safety factor		1.05
Design yield strength	MPa	438.1

Table 5
Mechanical characteristics of concrete (C32/40).

Property	Unit	Value
Cylindrical characteristic strength	MPa	32
Average cylindrical strength	MPa	40
Average tensile strength	MPa	3.02
Average flexural strength	MPa	3.63
Young's modulus	MPa	33,000
Cracked young's modulus	MPa	16,000
Cylindrical design strength	MPa	18.13
Design tensile strength	MPa	1.41

3.2. Numerical model of the bridge

The authors developed a 3D Finite Element model of the bridge (Fig. 3). 3D beam element model are used to model the main girders, cross beam, arch rib. Truss element model are used for braces and cables. Fig. 3 illustrates the numerical model with the supports used. The global model after discretization presents 430 nodes and 743 elements.

The structural elements such as arch ribs, beams, transverse beams, and transverse bracings are made of S420 steel, while S460 NL class steel is employed for the hangers. Additionally, C32/40 concrete with B450C steel reinforcements is used for the slab. The characteristics of these materials are detailed in Tables 3–6.

The characteristics of various bridge components are detailed in Table 7.

3.3. Assessment of the actions

To accurately model the static behavior of the bridge, the combined effects of various load cases were considered. These load cases include permanent loads, traffic load, and loads resulting from natural hazards such as wind and temperature fluctuations.

Table 6
Mechanical characteristics of concrete slab steel reinforcement (B450C).

Property	Unit	Value
Characteristic ultimate strength	MPa	540
Characteristic yield strength	MPa	450
Young's modulus	MPa	210,000
Design yield strength	MPa	391.3

Table 7
Section properties of the bridge components.

Component	Geometry	Values	Units	Diagram
Main girder	Total height (h)	2800	mm	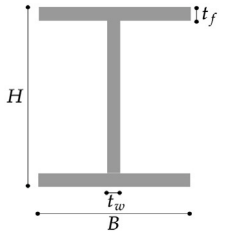
	Flange thickness (t_f)	40	mm	
	Flange width (b)	1000	mm	
	Web thickness (t_w)	40	mm	
	Area	189 000	mm^2	
	Moment of inertia	2.19×10^{11}	mm^4	
Cross beam	Total height (h)	600	mm	As above
	Flange thickness (t_f)	30	mm	
	Flange width (b)	300	mm	
	Web thickness (t_w)	15.5	mm	
	Area	27 000	mm^2	
	Moment of inertia	1.66×10^9	mm^4	
Arch Rib	Total height (H)	2000	mm	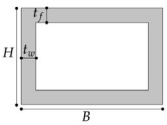
	Flange thickness (t_f)	35	mm	
	Width of section (B)	1500	mm	
	Web thickness (t_w)	30	mm	
Hangers	Diameter (H)	130	mm	Circular cross-section
	Cross section area	13 273.23	mm^2	
Bracing elements	Total height (H)	100	mm	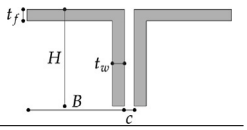
	Flange thickness (t_f)	10	mm	
	Width of section (B)	100	mm	
	Web thickness (t_w)	10	mm	
	Space (C)	10	mm	

Table 8
Self-weight of the structural elements.

Element	Cross-section area (m^2)	Characteristic value (kN/m)
Girder	0.1888	17.82
Cross Beam	0.0264	2.07
Arch Rib	0.2208	17.33
Bracing	0.0038	0.2983
Hanger	0.0134	1.0419
Concrete Slab	7.02	175.5

Table 9
Self-weight of the non-structural elements.

Elements	Number	Weight density (kN/m^3)	Width (m)	Characteristic value (kN/m)
Ballast	1	20	4	28
Sleepers (spacing = 0.6 m)	2 for both lanes	24 (Concrete sleepers)	2.6	3.96
Rails	2 per lane	–	–	2.4

The interaction of these loads was analyzed using the quasi-permanent combination approach for long-term effects, as expressed by the following equation:

$$\sum_j \left(G_{k,i} + P + \sum_{i \geq 1} \psi_{2,i} Q_{k,i} \right) \tag{23}$$

where $G_{k,i}$ represents the permanent loads, P denotes prestress, $\psi_{2,i}$ are the combination factors for variable loads, and $Q_{k,i}$ symbolizes the variable loads associated with each case.

The permanent loads include the self-weight of the main structural elements and the reinforced concrete slab. These weights are detailed in Table 8 and the weights of non-structural elements are grouped in Table 9.

This structure comprises two lanes, each with a width of 3 m and an axle spacing (approximately the standard rail spacings used) of 1435 mm, prescribed for normal railways. The railway traffic model adopted for the design is the standard Load Model

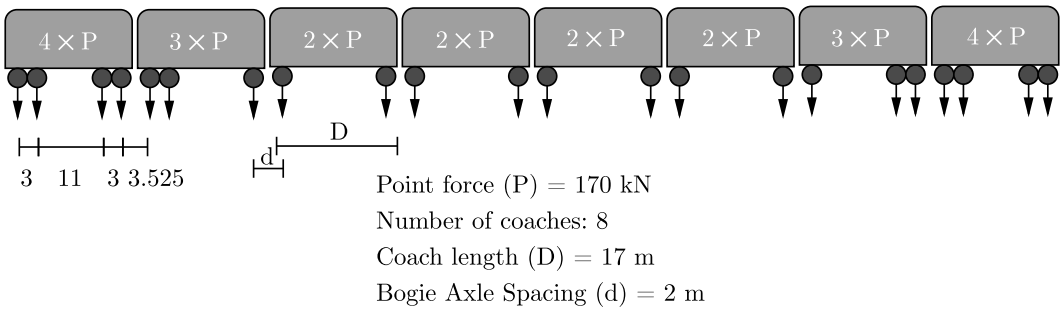

Fig. 4. High speed train load model HSLM-A1 according to Eurocode.

Table 10
Main effect of temperature load.

Parameter	Symbol	Value	Units
Maximum strain	ϵ	0.00018	
Maximum bridge elongation	ΔL	0.014	m

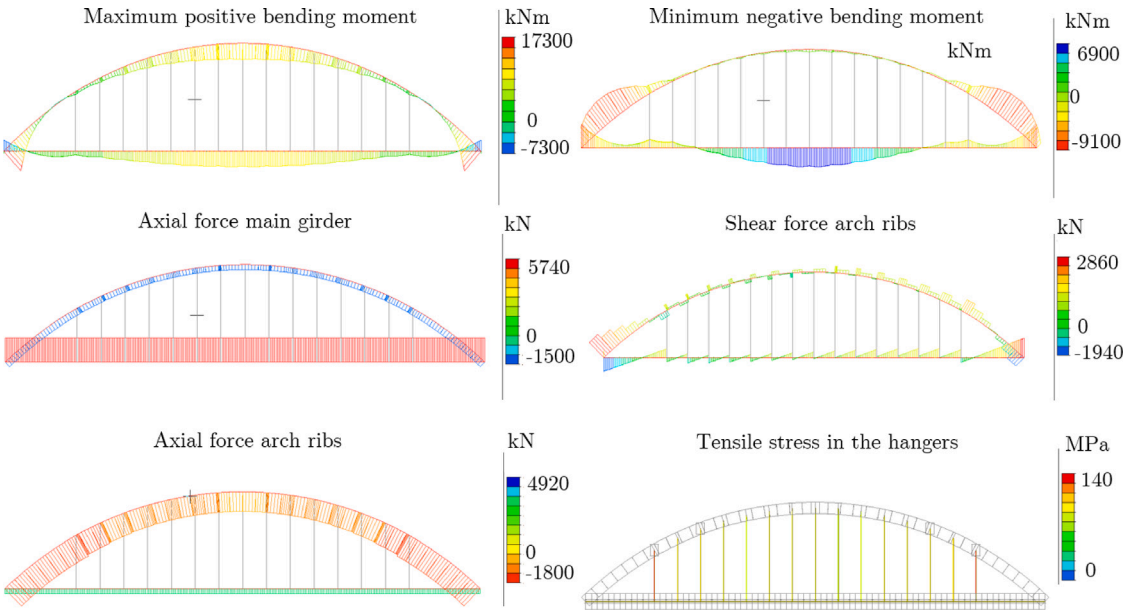

Fig. 5. Diagrams of the axial stress, shear force, and bending moment, with the maximum values from the fundamental load combination in the most significant structural elements.

HSLM A1, representing the loading from passenger trains at speeds exceeding 150 km/h. The model is predefined in the software Midas Civil and was calibrated, as detailed in Fig. 4.

The wind action has been computed according to the Italian standard [69], resulting of a wind distributed load of 4.1 kN/m.

The force due to temperature variation was determined based on available climatic data. A maximum positive temperature change of 20 °C and a minimum temperature change of −18° C were considered. Additionally, positive and negative temperature gradients of ±15 °C were applied to the bridge. The maximum effects of temperature load are detailed in Table 10.

3.4. Static analysis

The linear elastic analysis of the rail bridge was performed to assess the static performance of the structure under the influence of permanent loads. This analysis was carried out for validating the model and assessing the static stress state.

Given the predominance of stresses and strains in the vertical direction compared to other directions, only diagrams in the vertical direction will be presented. Fig. 5 displays diagrams of the axial stress, shear force, and bending moment, with the maximum values from the fundamental load combination in the most significant structural elements.

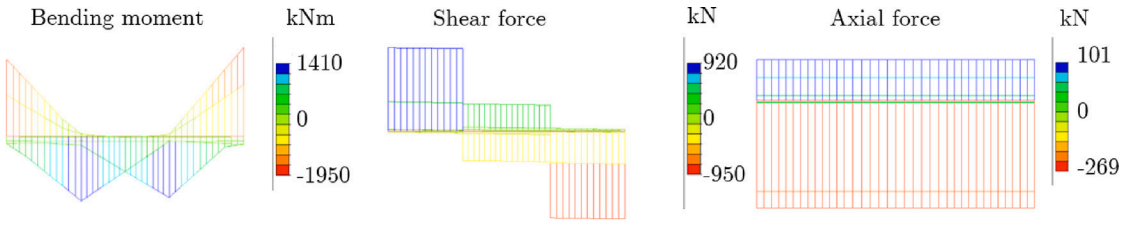

Fig. 6. Envelope of bending moment, shear and axial force in the cross beams.

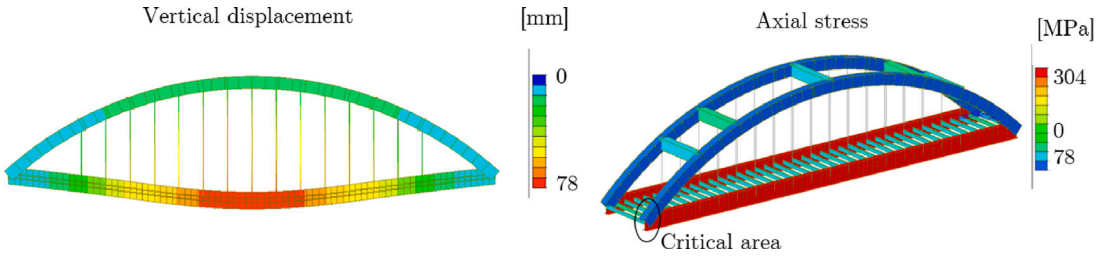

Fig. 7. Deformed shape of the bridge at the service limit state and identification of critical node characterized by the highest mechanical stresses.

Table 11
Stress values at the most critical joint.

Element	Girder	Cross beam
Axial stress (MPa)	304.06	−0.18
Shear stress in y direction (MPa)	103.93	0.13
Shear stress in z direction (MPa)	−36.08	498.13

The positive bending moment diagram shows the bending moment distribution across the arch. The maximum positive bending moment reaches up to 17300 kN m, which typically occurs near the supports where the reaction forces are greatest. The minimum negative moment (up to −9100 kN m) reveals tension on the inner curve of the arch, predominantly occurring at the crown of the arch. This is expected as the arch acts in compression at the supports and tension at the crown under vertical loading. The axial force in the main girder shows a predominant compressive force (up to 5740 kN), mainly due to thermal load. The axial forces in the arch ribs manifest a combination of tension and compression along the arch's length, with maximum compression at the ends near the supports and tension towards the middle. The maximum compression is around 4920 kN, and tension is about −1800 kN. This distribution is typical for arch structures. The shear forces in the arch ribs show significant variation, with maximum values up to 2860 kN and a minimum going down to −1940 kN. The highest shear occurs near the supports and reduces towards the apex of the arch. The hangers exhibit tensile stresses with a maximum stress of 140 MPa. The stress distribution is uneven, with the highest stress near the ends of the hangers where they connect to the arch and the deck. In conclusion, the highest bending moments occur at the supports and the crown, indicating that these are critical areas, especially in the design and inspection phases. Both axial and shear force distributions on the ribs reveal that the parts of the arch near the supports are the most stressed zones.

Fig. 6 displays the envelope of bending moment, shear and axial force in the cross beams. The bending moment diagram shows a "V" shape, due to the presence of point load. The maximum negative bending moment reaches about −1950 kN m, and a smaller positive moment of 1410 kN m, revealing that the crossbeams manifest more significant tension at the top fibers near the supports. The shear force diagram displays a stepped pattern, due to points of load application. The shear force varies from 920 kN to −950 kN. The positive and negative values indicate the direction of the shear force, which is crucial for determining the nature of the shear stresses and the necessary reinforcement in those areas. The axial force appears relatively uniform across the length of the crossbeams. However, there is a slight variation which might be due to the axial loads transmitted from other connected structural components like arches or the main girders. Axial forces show a maximum compressive force of about −269 kN and a minor tensile force up to 101 kN.

Regarding the bridge deflection, the maximum deflection at the service limit state is 78 mm, which is less than the limit $L/500$ = 157 mm, according to the Eurocode [70], see Fig. 7(a). The deflection calculation has been carried out considering the effect of shear strain.

In conclusion, the most critical area of the bridge is the approach zone where the connection between the main girder and the cross-beam, circled in Fig. 7(b). As will be detailed later, the evaluation of the bridge's fatigue response will focus on the analysis of this structural node, being the most vulnerable part of the structure.

This joint is at the intersection of the cross beam and the girder. The numerical values of the stresses for each of these elements are detailed in Table 11.

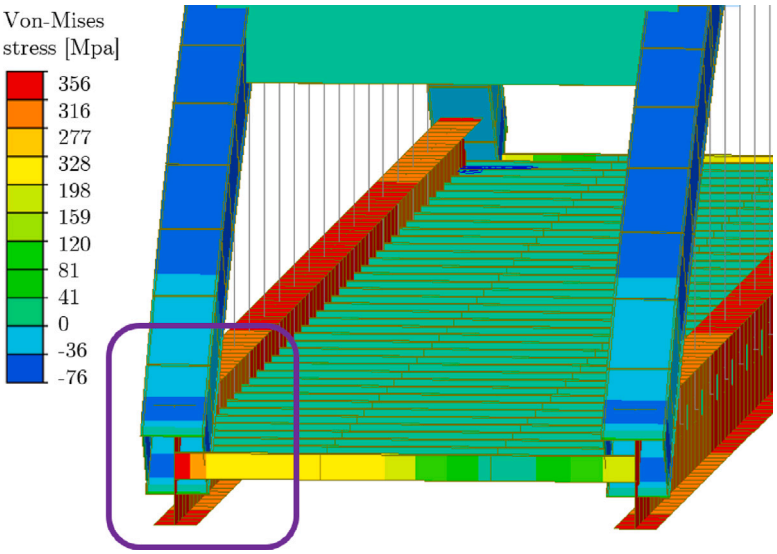

Fig. 8. Von-Mises stress of the most stressed joint, shown by the rectangle.

Table 12
Frequency of vibration and corresponding critical velocities.

Frequency of vibration [Hz]	Critical velocity [km/h]
9.89	332
10.96	368
12.21	410
14.81	498
16.01	540
20.81	700

The stress distribution can be better appreciated from Fig. 8.

3.5. Modeling the dynamic load effects

For the fatigue response evaluation of the bridge, it is necessary to consider the dynamic effects of the traveling load. In the case study considered, the authors have neglected the effects of vehicle–structure interaction due to their modest nature. This is explained by two reasons. In railway bridges, the roughness of the rails is very low and thus negligible compared to that of roads [71]. Furthermore, the speed of the train is far from the critical speed defined in the same way ($c_{cr,i}$) as follows [72]:

$$c_{cr,i} = \frac{S \cdot \omega_i \cdot l}{\pi} \tag{24}$$

where ω_i is the ith natural pulsation, S is the speed parameter of the train, and l its length. The speed parameter S is taken to be equal to $0.25d/L$, which corresponds to 0.375.

Table 12 shows the critical velocities obtained for the various modes, as reported in Fig. 9. By keeping the train speed not exceeding 200 km/h, resonance effects are negligible, and thus the traveling load can be modeled as moving point loads.

In conclusion, for the evaluation of the mechanical response of the node, the authors studied the bridge's response under a traveling block load, defined in Fig. 4, disregarding any vehicle–bridge interaction, which is of little significance for these structures as demonstrated in many studies [73]. The block load is modeled as a sequence of concentrated forces moving at a constant speed.

3.6. Refined modeling of the bolted joint

For a more accurate assessment of the stress state at the critical node of the structure, located at the intersection between the main girder and the cross-beam, the authors conducted a detailed FE modeling. This included modeling of the bolts and drilled flanges, to account for stress concentrations at the bolted joints.

Tables 13 and 14 characterize the geometric and mechanical properties of the steel plates and bolts used in the assemblies, shown in Fig. 10.

Fig. 11 displays the refined FE model of the bolted joint for fatigue life assessment.

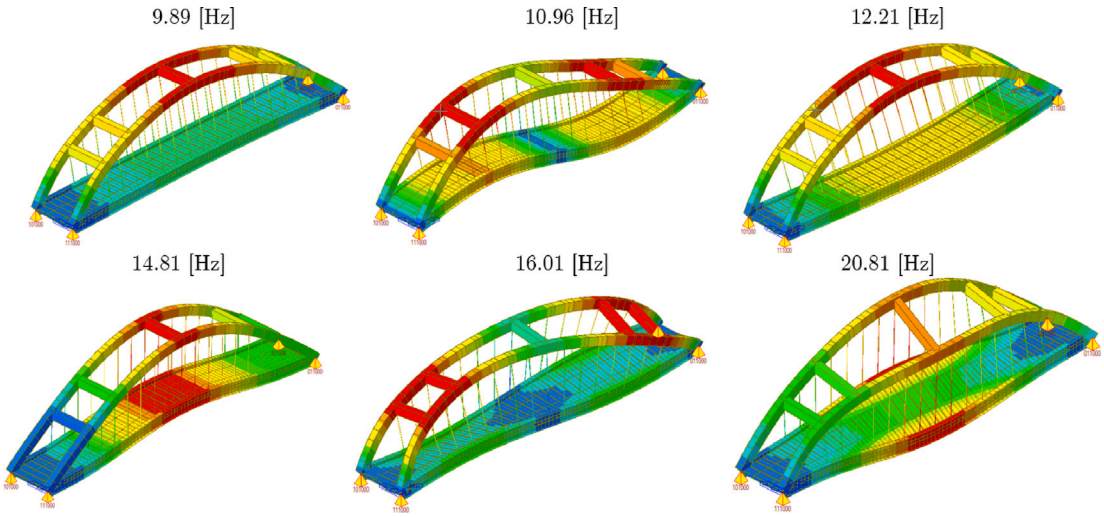

Fig. 9. View of the first six modes of the structure.

Table 13
Characteristics of plate.

Element	Thickness [mm]	Width [mm]	Material
Plate	20	150	S420

Table 14
Characteristics of bolts, where f_{yb} and f_{ub} are the yielding and ultimate strengths, respectively.

Bolt class	f_{yb} [MPa]	f_{ub} [MPa]	Diameter [mm]	Hole diameter [mm]
Bolt M24	900	1000	24	26
Bolt M27	900	1000	27	30

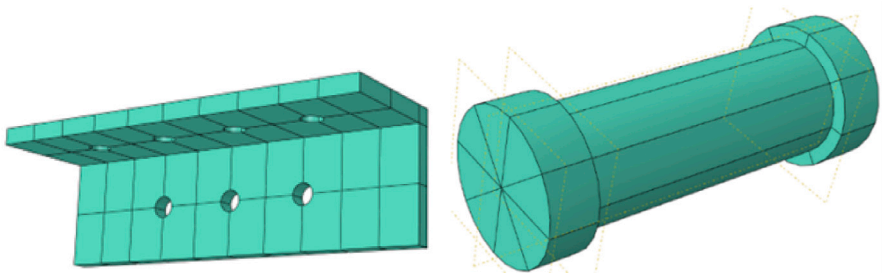

Fig. 10. FE model of the plate and the bolt.

4. Fatigue life assessment

As anticipated in the previous section, the maximum and minimum stresses were identified after a refined FE analysis on the joint between the cross beam element and the main girder, as shown in Fig. 12.

The stress plot shows that the most stressed element of the node are on the plates, close to the bolts.

Table 15 lists the mechanical properties of steel used in multiaxial fatigue criteria defined in Section No. 2.

Fig. 13(a) displays the time histories of axial and shear stress at the most stressed point under the train load, as defined in Fig. 4. The passage of the train induces higher shear stress compared to axial stress. Specifically, the time histories exhibit higher peaks at the beginning due to the greater load exerted by the locomotive, which then decreases in subsequent carriages. When plotting stress versus strain, no nonlinearity is observed, see Fig. 13(b). The variations remain within the elastic range, while being proportional.

Table 16 and Fig. 14 provide estimates of fatigue life using the considered fatigue criteria, illustrating diverse approaches to evaluating the endurance of structural components under repeated loading.

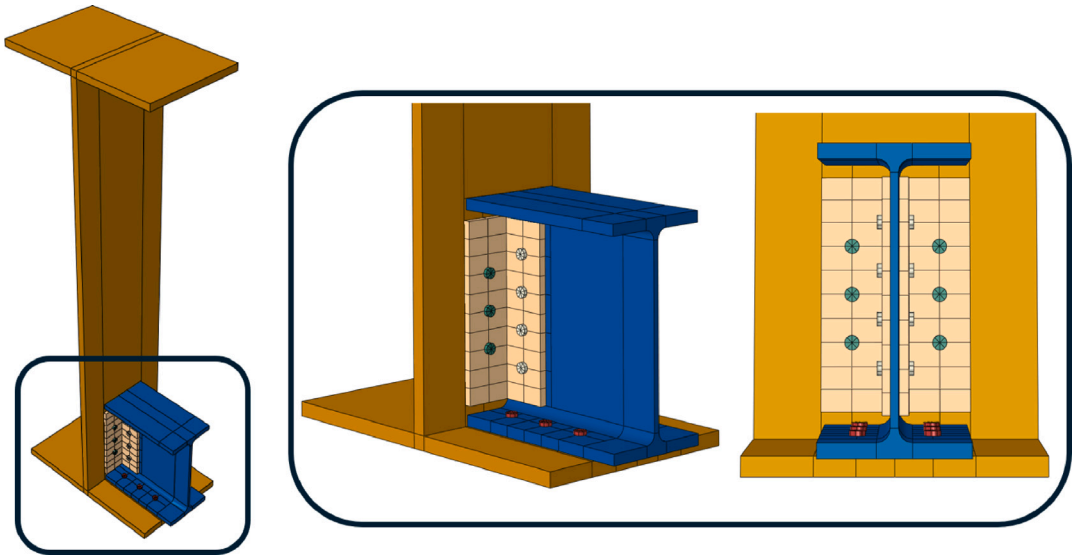

Fig. 11. Refined FE model of the bolted joint characterized by the most severe stress state.

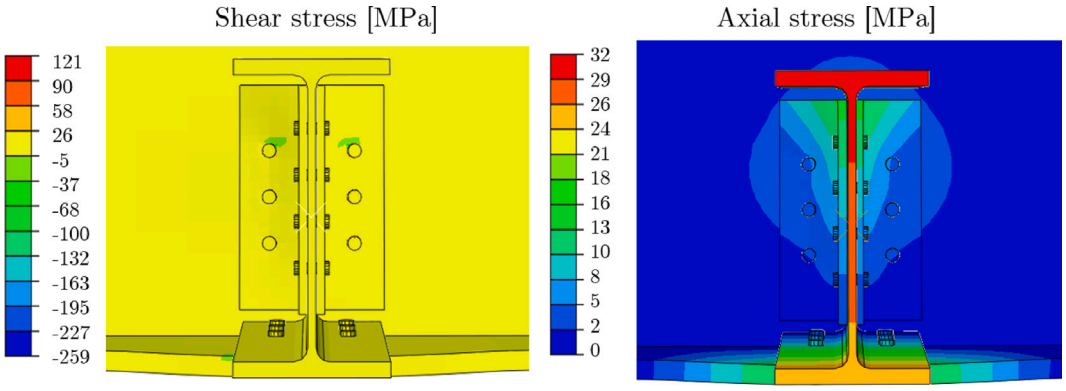

Fig. 12. Nephogram of the (a) shear and (b) axial stresses of the most critical joint under investigation.

Table 15
Mechanical properties of steel used in multiaxial fatigue criteria [60].

Property	Value
Young's modulus E (Pa)	210×10^9
Fatigue tensile strength σ'_f (Pa)	1190×10^6
Tensile yield strength σ_y (Pa)	450×10^6
Shear modulus G (Pa)	81.2×10^9
Fatigue shear strength τ'_f (Pa)	$0.6 \times \sigma'_f$
Fatigue strength exponent b	−0.087
Fatigue ductility exponent c	−0.53
Material-dependent constant S_k for KBM [61]	0.9
Fatemi–Socie constant k	0.3
Fatigue tensile strain ϵ'_f	0.12
Fatigue shear strain γ'_f	0.12

The low-cycle fatigue results (SWT, KBM, Glinka, FS) show much shorter fatigue life predictions than the high-cycle fatigue criteria (Crossland, Basquin, EC3, BS). This is expected because low-cycle fatigue focuses on conditions where plastic deformation occurs under higher strain amplitudes, leading to faster fatigue failure. Conversely, high-cycle fatigue methods assume elastic deformation and lower strain amplitudes, resulting in significantly longer predicted fatigue lives. These are more appropriate when the structure is subjected to millions of cycles with relatively low stresses. However, some low-cycle criteria predictions are not very far from those of standard high-cycle predictions (such as EC3 and BS). KBM is the most conservative low-cycle fatigue method

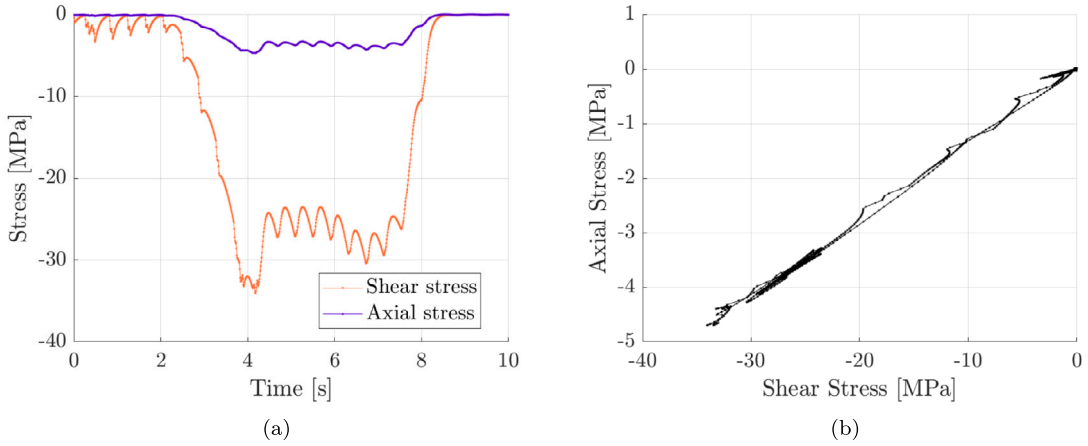

Fig. 13. (a) Time history of the axial and shear stresses, (b) Axial vs. Shear stress plot.

Table 16
Number of train transit to failure according to all considered damage criteria (the reference train is shown in Fig. 4). The fatigue life is estimated considering 30 train transits per day.

Fatigue assessment	Low-cycle fatigue				High-cycle fatigue			
	SWT [59]	KBM [61]	Glinka [29]	FS [63]	Crossland [24]	Basquin [65]	EC3 [66]	BS [67]
1/D[a]	1.16E+06	3.01E+05	2.04E+06	1.32E+06	1.63E+07	1.91E+07	3.66E+06	3.94E+07
Fatigue life [years]	105.48	27.52	186.52	120.52	1491.39	1740.03	334.44	359.91

[a] Number of train transit to failure.

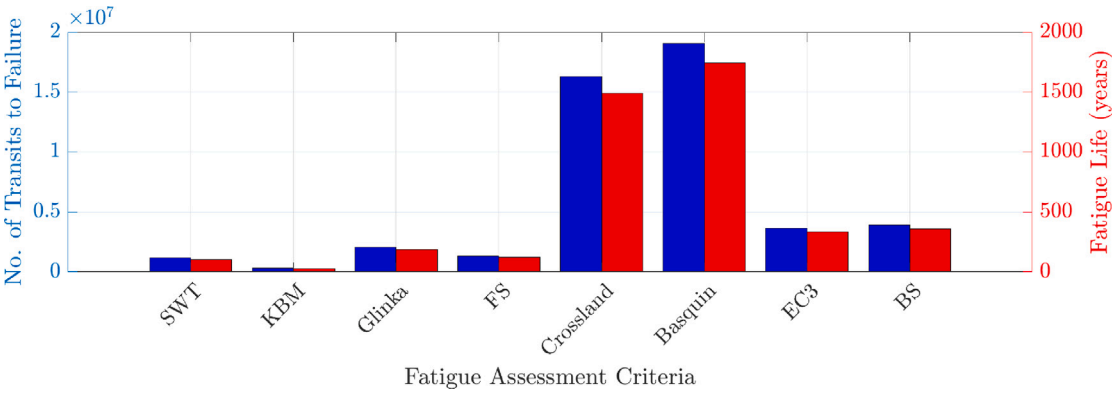

Fig. 14. Bar plot of the number of train transit to failure according to all considered damage criteria (the reference train is shown in Fig. 4). The fatigue life (right *y*-axis) is estimated considering 30 train transits per day.

among low-cycle criteria, likely due to its emphasis on multiaxial stress and strain states. It predicts the earliest failure and may not be considered reliable in this context. Basquin and Crossland provide relatively optimistic fatigue life estimates, around 1400 and 1500 years, respectively. Crossland's prediction is slightly lower because it includes multiaxial stress states, considering the second invariant of the deviatoric stress tensor and the maximum hydrostatic stress. The very high estimates are because the parameters used are calibrated for average predictions, which correspond to a 50% failure probability. The Eurocode estimates seem more realistic, but they are based on a lower probability of failure, for example, 2.3% in the case of the BS standard. These standards are specifically designed for steel structures and railway bridges, making them reliable benchmarks for comparison. Their results suggest the bridge will experience a long fatigue life under the current loading conditions. Interestingly, when higher failure probability is considered for BS, the estimates approximate those of Crossland and Basquin exceeding 1500 years.

Given the long predicted fatigue lives, the structure's loading seems to fall under high-cycle fatigue conditions, where stress remains in the elastic range. EC 3 and BS might provide the most realistic estimations, as they are tailored for railway bridges and civil structures. It is also worth noting that the estimates from the standards, which are inherently reduced to account for lower probabilities of failure, are very close to the deterministic values obtained from the low-cycle fatigue criteria. While low-cycle fatigue

Table 17
Fixed and variable parameters on the univariate sensitivity analysis.

Variable parameters				Constant parameters	
Speeds [km/h]				Axle load [kN]	Convoy length [m]
150	170	190	210	170	179
Axle load [kN]				Speeds [km/h]	Convoy length [m]
170	190	210	230	170	179
Convoy length [m]				Speeds [km/h]	Axle load [kN]
213	247	281	315	247	170

Table 18
Results of univariate sensitivity analysis. The table displays the number of cycles to failure for the considered three traffic parameters' variation.

Velocity [km/h]	Low-cycle fatigue criteria				High-cycle fatigue criteria			
	SWT	KBM	Glinka	FS	Crossland	Basquin	EC3	BS
150	2.44E+06	1.53E+05	4.31E+06	2.22E+06	1.63E+07	1.91E+07	3.66E+06	3.94E+06
170	"	"	"	"	"	"	"	"
190	"	"	"	"	"	"	"	"
210	"	"	"	"	"	"	"	"
Axle load [kN]	SWT	KBM	Glinka	FS	Crossland	Basquin	EC3	BS
170	2.44E+06	1.53E+05	4.31E+06	2.22E+06	1.63E+07	1.91E+07	3.66E+06	3.94E+06
190	"	1.24E+05	"	"	1.10E+07	1.09E+07	1.83E+06	1.58E+06
210	"	9.53E+04	"	"	5.65E+06	4.69E+06	1.21E+06	1.26E+06
230	"	6.63E+04	"	"	1.63E+06	1.72E+06	4.39E+05	5.91E+05
Convoy length [m]	SWT	KBM	Glinka	FS	Crossland	Basquin	EC3	BS
213	2.12E+06	1.41E+05	3.96E+06	2.12E+06	2.36E+07	2.56E+07	5.16E+06	5.48E+06
247	1.79E+06	1.28E+05	3.60E+06	1.94E+06	1.88E+07	2.01E+07	4.10E+06	4.37E+06
281	1.47E+06	1.16E+05	3.24E+06	1.75E+06	1.41E+07	1.46E+07	3.11E+06	3.27E+06
315	1.15E+06	1.03E+05	2.89E+06	1.17E+06	9.42E+06	9.09E+06	2.01E+06	2.09E+06

criteria may not be as relevant, they become more applicable when axle loads increase, bringing stresses closer to the plastic limit. Under such conditions, these criteria provide reasonable and comparable estimates to the standards, as discussed in the following section.

5. Univariate sensitivity analysis of fatigue life to traffic variables

The authors conducted a univariate sensitivity analysis to quantify the effects of traffic parameters, namely velocity, axle load, and train length. Specifically, they performed three analyses by varying one parameter at a time while fixing the other two, as reported in Table 17.

Four numerical models have been developed to analyze the influence of train velocity variation on the bridge's dynamic response. These models simulate trains of the same length and axle load but with varying velocities of 150 km/h, 170 km/h, 190 km/h, and 210 km/h. These specific values were selected to remain below the critical velocity of 332 km/h. Additionally, the impact of varying axle loads was assessed by adopting the following axle load configurations: AL1 (190 kN), AL2 (210 kN), and AL3 (230 kN). To account for variations in train length, the authors considered increases of 2, 4, 6, and 8 wagons, respectively, in the model simulations.

Fig. 15 presents the time histories of axial and shear stresses for three parametric analyses: (a) velocity, (b) axle load, and (c) train length. Each subfigure displays the time history on the left and the shear versus axial stress on the right. The stress values are substantially independent of the velocity, which, except for the duration of the time history, yields nearly identical stress values and number of cycles. Regarding the axle load, it induces a significant variation in stress, particularly the peak corresponding to the locomotive's transit, which rises from 30 to almost 50 MPa. Nevertheless, the response remains within the elastic range, and the shear and axial stresses and strains are proportional to each other. The increment in train length leads to a higher number of cycles, which indirectly reduces the total number of train transits to failure (see Table 18).

As depicted in Fig. 15, the time histories have reflected the results.

Notably, no effect of train velocity on fatigue life is observed within the considered ranges. The damage criteria do not account for the deformation rate but focus solely on stress levels and the number of cycles, which remain substantially unchanged, thus yielding the same values when numerically solving the equations that express the damage criterion. The number of cycles to failure decreases as the axle load increases. This trend is observed across both low-cycle and high-cycle fatigue criteria. Regarding the axle load, the predictions from the low-cycle criteria, such as SWT and FS, remain substantially unchanged. The only criteria showing variation are KBM and all high-cycle fatigue criteria. Specifically, KBM and Crossland appear quite sensitive to variations in shear stresses. The convoy length has an almost proportional effect on the number of cycles to failure. Similarly, EC3 and BS 5400 show a decreasing trend with increasing axle load and convoy length. However, their results remain more consistent than Crossland's, making them more reliable for design purposes. Convoy length also influences fatigue life, with longer convoys leading to fewer cycles to failure.

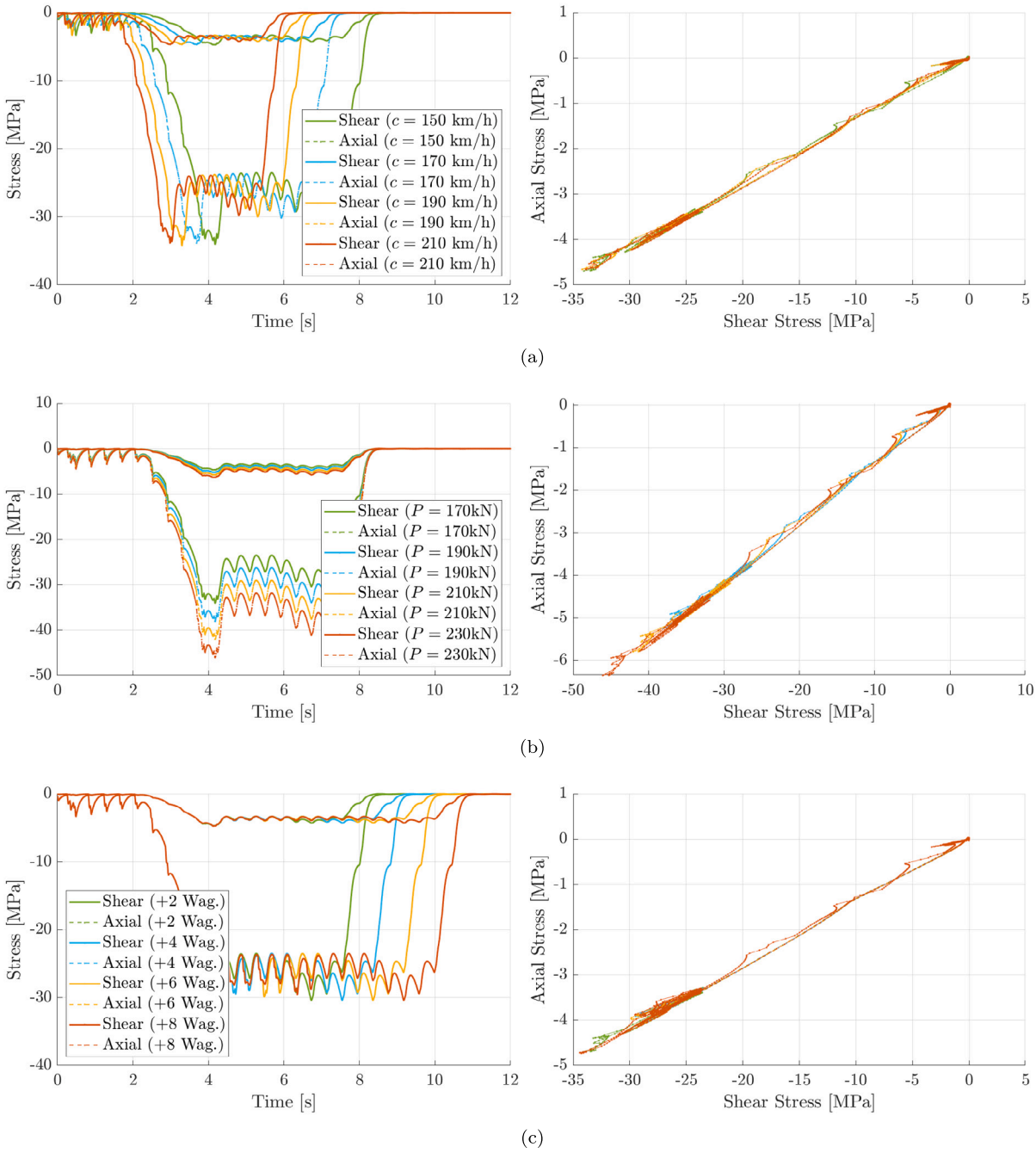

Fig. 15. (right) Time history of the axial and shear stresses, (left) Axial vs. Shear stress plot. (a) shows the variation due to train velocity, (b) due to axle load and (c) the convoy length.

This is observed in low-cycle and high-cycle criteria but with a minor effect compared to axle loads. In conclusion, the results are quite variable. In this specific case, the use of high-cycle fatigue criteria is recommended. However, given the moderate stress levels (e.g., an axial stress range of 50 MPa), the predictions from low-cycle fatigue criteria are very close to those from the high-cycle criteria provided by the standards, which are generally associated with predictions for lower probabilities of failure. Considering about 30 trains per day, representing a typical scenario for a medium-traffic railway line, an estimated lifespan of approximately 100–300 years aligns with several studies in the literature, such as in [74].

Specifically, Su et al. [74] study a steel arch bridge similar to the one under investigation, supported by cables, and estimate the probability of fatigue failure over the years, limiting their analysis to 100 years. In some cases (see case No. 1 in [74]), there

is a 100% probability of failure by the 100th year. In previous studies on bridges of different types, such as [75,76], the lifespan estimates are similar, in the range of 50–100 years, which is the range found for higher axle loads.

6. Conclusions

The work compares various multiaxial damage criteria for the fatigue life assessment of railway steel bridges. Evaluating fatigue life involves three main steps: a method for counting load cycles, damage creation, and damage accumulation mechanisms.

Given that this involves train loads rather than sinusoidal excitation, the authors implemented the rainflow method as defined in the ASTM E1049-85 (2011) standard [20]. Six damage criteria were compared to evaluate their performance on railway bridges, as most literature applies these methods primarily to other engineering fields such as aircraft and automotive.

The authors compared the predictions of low- and high-cycle fatigue criteria since, although the stress state is in the elastic range, it is moderate and could lead to an intermediate situation between low- and high-cycle fatigue, which needs to be verified and analyzed. The low-cycle criteria used are Smith–Watson–Topper (SWT) [59], Kandil, Brown, and Miller (KBM) [61], Glinka [29], and Fatemi and Socie (FS) [63]. The high-cycle criteria include Crossland [24], Basquin [65], and the methods recommended by Eurocode 3 [66] and the British Standard [67]. Miner's rule was then adopted to quantify damage accumulation.

The selected case study is a steel arch bridge over the Polcevera River in Genoa, Italy. The bridge was modeled in Midas Civil, and fatigue analysis was conducted on the most stressed structural node, a bolted joint connecting the main girder and the cross-beam. Load histories in terms of stress and strain were used to quantify the fatigue life of the joint. The railway load was modeled as a train of concentrated loads, neglecting vehicle–bridge interaction due to its irrelevance in this case, given the low rail roughness and the train speed being well below the critical speed. The values for vertical accelerations and maximum bending stresses are below the standard EN 1994-2 limits.

The bridge's response remains predominantly within the elastic range. Therefore, the recommended high-cycle criteria provide more reliable estimates. In particular, Crossland and Basquin predict a fatigue life greater than 1000 years, while the British Standard and Eurocode predict approximately 300 years. This discrepancy arises because the standards are based on lower failure probabilities and tend to provide conservative estimates. In contrast, the predictions from Basquin and Crossland can be considered mean estimates associated with a 50% probability of failure. Considering about 30 trains per day, which represents a typical scenario for a medium-traffic railway line, an estimated lifespan of approximately 300 years, according to the Standards, aligns with several studies in the literature with similar bridge typologies. The predictions are significantly lower for the low-cycle criteria. Still, except for KBM, which tends to underestimate fatigue life severely, the estimates are not far below the standards, ranging from approximately 100 to 200 years.

In a second step, a univariate sensitivity analysis was conducted to evaluate the sensitivity of fatigue life to certain traffic parameters, such as axle load, velocity, and train length. No effect of train velocity on fatigue life is observed within the considered ranges. Both low-cycle and high-cycle fatigue criteria display consistent trends regarding the impact of axle load and convoy length. Still, high-cycle fatigue criteria (Crossland, Basquin, EC3, BS) predict longer fatigue lives than low-cycle criteria.

CRediT authorship contribution statement

Emanuele Maiorana: Writing – review & editing, Visualization, Supervision, Resources, Project administration, Funding acquisition, Formal analysis, Data curation, Conceptualization. **Angelo Aloisio:** Writing – original draft, Validation, Software, Methodology, Investigation, Formal analysis, Data curation, Conceptualization. **Valdinique Tasse:** Writing – original draft, Software, Investigation, Formal analysis, Data curation. **Bruno Briseghella:** Writing – review & editing, Visualization, Validation, Supervision, Methodology.

Declaration of competing interest

All authors have participated in (a) conception and design, or analysis and interpretation of the data; (b) drafting the article or revising it critically for important intellectual content; and (c) approval of the final version.

This manuscript has not been submitted to, nor is under review at, another journal or other publishing venue.

The authors have no affiliation with any organization with a direct or indirect financial interest in the subject matter discussed in the manuscript

Data availability

Data will be made available on request.

Acknowledgment

The authors would like to express their gratitude to Franck Kenneth for the Polcevera bridge photo.

References

[1] G. Kuitche, Paramétrage de la Réponse Dynamique des Ponts Rail sous Trafic Ferroviaire Master's thesis, National Advance School of Public Works, Cameroon, 2021, Master of Engineering (Meng) in Civil Engineering.

[2] R. Oshiro, M. Alves, Predicting the behaviour of structures under impact loads using geometrically distorted scaled models, J. Mech. Phys. Solids 60 (7) (2012) 1330–1349.

[3] M. Simoncelli, A. Aloisio, M. Zucca, G. Venturi, R. Alaggio, Intensity and location of corrosion on the reliability of a steel bridge, J. Constr. Steel Res. 206 (2023) 107937.

[4] R. Cucuzza, A. Aloisio, R. Di Bari, M. Domaneschi, Vulnerability assessment and lifecycle analysis of an existing masonry arch bridge, Eng. Struct. 302 (2024) 117422.

[5] A. Aloisio, D.P. Pasca, R. Alaggio, M. Fragiacomo, Bayesian estimate of the elastic modulus of concrete box girders from dynamic identification: A statistical framework for the A24 motorway in Italy, Struct. Infrastruct. Eng. 17 (12) (2021) 1626–1638.

[6] R. Fincato, S. Tsutsumi, H. Momii, Ductile damage evolution under cyclic non-proportional loading paths, Procedia Struct. Integr. 9 (2018) 136–150.

[7] D. Trenton, M. Bianca, The past, present, and future of experimental methods in the social sciences, Soc. Sci. Res. 108 (2022) 102799.

[8] X. Chengshun, Z. Zihong, L. Yang, D. Xiuli, Validation of a numerical model based on dynamic centrifuge tests and studies on the earthquake damage mechanism of underground frame structures, Tunn. Undergr. Space Technol. 104 (2020) 103538.

[9] X. Ye, Y. Su, J. Han, A state-of-the-art review on fatigue life assessment of steel bridges, Math. Probl. Eng. 2014 (1) (2014) 956473.

[10] B. Briseghella, C. Lan, E. Mazzarolo, E. Siviero, T. Zordan, Fatigue assessment on fork end connectors in a cable structure, in: Proceedings of the 35th Annual Symposium of IABSE / 52nd Annual Symposium of IASS / 6th International Conference on Space Structures: Taller, Longer, Lighter - Meeting Growing Demand with Limited Resources, IABSE-IASS 2011 London Symposium Report, London, United Kingdom, 2011.

[11] H. Altenbach, A. Zolochevsky, Generalized fatigue limit criterion and unified theory of low cycle fatigue damage, Fatigue Fract. Eng. Mater. Struct. 19 (10) (1996) 1207–1219.

[12] J. Lemaitre, J.-L. Chaboche, Mechanics of Solid Materials, 1994.

[13] M. Meggiolaro, J. De Castro, An improved multiaxial rainflow algorithm for non-proportional stress or strain histories - part II: The modified wang-brown method, Int. J. Fatigue 42 (2012) 194–206, http://dx.doi.org/10.1016/j.ijfatigue.2011.10.012, cited By 70.

[14] M. Meggiolaro, J. De Castro, An improved multiaxial rainflow algorithm for non-proportional stress or strain histories - Part I: Enclosing surface methods, Int. J. Fatigue 42 (2012) 217–226, http://dx.doi.org/10.1016/j.ijfatigue.2011.10.014, cited By 79.

[15] R. Brighenti, A. Carpinteri, A notch multiaxial-fatigue approach based on damage mechanics, Int. J. Fatigue 39 (2012) 122–133, http://dx.doi.org/10.1016/j.ijfatigue.2011.02.003, cited By 55.

[16] Z. Wei, P. Dong, A rapid path-length searching procedure for multi-axial fatigue cycle counting, Fatigue Fract. Eng. Mater. Struct. 35 (6) (2012) 556–571, http://dx.doi.org/10.1111/j.1460-2695.2012.01649.x, cited By 20.

[17] Z. Wei, P. Dong, Multiaxial fatigue life assessment of welded structures, Eng. Fract. Mech. 77 (15) (2010) 3011–3021, http://dx.doi.org/10.1016/j.engfracmech.2010.03.045, cited By 53.

[18] H. Chen, D.-G. Shang, E.-T. Liu, Multiaxial fatigue life prediction method based on path-dependent cycle counting under tension/torsion random loading, Fatigue Fract. Eng. Mater. Struct. 34 (10) (2011) 782–791, http://dx.doi.org/10.1111/j.1460-2695.2011.01572.x, cited By 18.

[19] N.D. Bibbo, M.L.v. Larsen, J. Baumgartner, V. Arora, An improved rainflow counting method for multiaxial stress states using the minimum circumscribed circle method to identify shear stress ranges, Int. J. Fatigue 163 (2022) 106997.

[20] ASTM E1049-85 (2011) standard practices for cycle counting in fatigue analysis, 2011, http://dx.doi.org/10.1520/E1049-85R11, URL https://www.astm.org/e1049-85r11.html.

[21] N. Shamsaei, A. Fatemi, Effect of hardness on multiaxial fatigue behaviour and some simple approximations for steels, Fatigue Fract. Eng. Mater. Struct. 32 (8) (2009) 631–646, http://dx.doi.org/10.1111/j.1460-2695.2009.01369.x, cited By 107.

[22] L. Susmel, P. Lazzarin, A bi-parametric Wöhler curve for high cycle multiaxial fatigue assessment, Fatigue Fract. Eng. Mater. Struct. 25 (1) (2002) 63–78, http://dx.doi.org/10.1046/j.1460-2695.2002.00462.x, cited By 246.

[23] D. McDiarmid, A general criterion for high cycle multiaxial fatigue failure, Fatigue Fract. Eng. Mater. Struct. 14 (4) (1991) 429–453, http://dx.doi.org/10.1111/j.1460-2695.1991.tb00673.x, cited By 309.

[24] B. Crossland, Effect of large hydrostatic pressures on the torsional fatigue strength of an alloy steel, Proc. Int. Conf. Fatigue Metals (1956) 138–149, cited By 491.

[25] M. Brown, K. Miller, A theory for fatigue failure under multiaxial stress-strain conditions, Proc. Inst. Mech. Eng. 187 (65) (1973) 745–755, cited By 890.

[26] A. Fatemi, D. Socie, A critical plane approach to multiaxial fatigue damage including out-of-phase loading, Fatigue Fract. Eng. Mater. Struct. 11 (3) (1988) 149–165, http://dx.doi.org/10.1111/j.1460-2695.1988.tb01169.x, cited By 1603.

[27] J. Li, Z.-p. Zhang, Q. Sun, C.-w. Li, Y.-j. Qiao, A new multiaxial fatigue damage model for various metallic materials under the combination of tension and torsion loadings, Int. J. Fatigue 31 (4) (2009) 776–781, http://dx.doi.org/10.1016/j.ijfatigue.2008.03.008, cited By 53.

[28] K. Smith, P. Watson, T. Topper, Stress- strain function for the fatigue of metals, J. Mater. 5 (4) (1970) 767–778, cited By 2338.

[29] G. Glinka, G. Shen, A. Plumtree, A multiaxial fatigue strain energy density parameter related to the critical fracture plane, Fatigue Fract. Eng. Mater. Struct. 18 (1) (1995) 37–46, http://dx.doi.org/10.1111/j.1460-2695.1995.tb00140.x, cited By 192.

[30] A. Varvani-Farahani, New energy-critical plane parameter for fatigue life assessment of various metallic materials subjected to in-phase and out-of-phase multiaxial fatigue loading conditions, Int. J. Fatigue 22 (4) (2000) 295–305, http://dx.doi.org/10.1016/S0142-1123(00)00002-5, cited By 194.

[31] D. Socie, Multiaxial fatigue damage models, J. Eng. Mater. Technol. Trans. ASME 109 (4) (1987) 293–298, http://dx.doi.org/10.1115/1.3225980, cited By 633.

[32] K. Liu, Method based on virtual strain-energy parameters for multiaxial fatigue life prediction, (1191) 1993, pp. 67–84, cited By 151,

[33] I. Papadopoulos, P. Davoli, C. Gorla, M. Filippini, A. Bernasconi, A comparative study of multiaxial high-cycle fatigue criteria for metals, Int. J. Fatigue 19 (3) (1997) 219–235, http://dx.doi.org/10.1016/S0142-1123(96)00064-3, cited By 521.

[34] C. Sonsino, Overview of the state of the art on multiaxial fatigue of welds, in: Proceedings of the 5th International Conference on Biaxial/Multiaxial Fatigue & Fracture, Vol. 1, 1997, pp. 395–419, cited By 10.

[35] M. Brown, K. Miller, Two decades of progress in the assessment of multiaxial low-cycle fatigue life, STP 770, 1982, pp. 482–499, http://dx.doi.org/10.1520/STP32442S, cited By 104,

[36] B.-R. You, S.-B. Lee, A critical review on multiaxial fatigue assessments of metals, Int. J. Fatigue 18 (4) (1996) 235–244, http://dx.doi.org/10.1016/0142-1123(96)00002-3, cited By 302.

[37] E. Macha, C. Sonsino, Energy criteria of multiaxial fatigue failure, Fatigue Fract. Eng. Mater. Struct. 22 (12) (1999) 1053–1070, http://dx.doi.org/10.1046/j.1460-2695.1999.00220.x, cited By 183.

[38] Y.-Y. Wang, W.-X. Yao, Evaluation and comparison of several multiaxial fatigue criteria, Int. J. Fatigue 26 (1) (2004) 17–25, http://dx.doi.org/10.1016/S0142-1123(03)00110-5, cited By 193.

[39] T. Chakherlou, Y. Alvandi-Tabrizi, A. Kiani, On the fatigue behavior of cold expanded fastener holes subjected to bolt tightening, Int. J. Fatigue 33 (6) (2011) 800–810, http://dx.doi.org/10.1016/j.ijfatigue.2010.12.014, cited By 59.

[40] A. Varvani-Farahani, T. Kodric, A. Ghahramani, A method of fatigue life prediction in notched and un-notched components, J. Mater. Process. Technol. 169 (1) (2005) 94–102, http://dx.doi.org/10.1016/j.jmatprotec.2005.01.015, cited By 28.
[41] Y. Jiang, O. Hertel, M. Vormwald, An experimental evaluation of three critical plane multiaxial fatigue criteria, Int. J. Fatigue 29 (8) (2007) 1490–1502, http://dx.doi.org/10.1016/j.ijfatigue.2006.10.028, cited By 183.
[42] M. Miner, Cumulative damage in fatigue, J. Appl. Mech. Trans. ASME 12 (3) (1945) A159–A164, http://dx.doi.org/10.1115/1.4009458, cited By 5026.
[43] D. Socie, G. Marquis, Multiaxial Fatigue (2000) cited By 838.
[44] A. Carpinteri, A. Spagnoli, S. Vantadori, C. Bagni, Structural integrity assessment of metallic components under multiaxial fatigue: The C-S criterion and its evolution, Fatigue Fract. Eng. Mater. Struct. 36 (9) (2013) 870–883, http://dx.doi.org/10.1111/ffe.12037, cited By 111.
[45] A. Carpinteri, A. Spagnoli, Multiaxial high-cycle fatigue criterion for hard metals, Int. J. Fatigue 23 (2) (2001) 135–145, http://dx.doi.org/10.1016/S0142-1123(00)00075-X, cited By 303.
[46] T. Chakherlou, M. Mirzajanzadeh, B. Abazadeh, K. Saeedi, An investigation about interference fit effect on improving fatigue life of a holed single plate in joints, Eur. J. Mech. A Solids 29 (4) (2010) 675–682, http://dx.doi.org/10.1016/j.euromechsol.2009.12.009, cited By 109.
[47] F. Esmaeili, T. Chakherlou, M. Zehsaz, S. Hasanifard, Investigating the effect of clamping force on the fatigue life of bolted plates using volumetric approach, J. Mech. Sci. Technol. 27 (12) (2013) 3657–3664, http://dx.doi.org/10.1007/s12206-013-0911-3, cited By 22.
[48] K. Iyer, C. Rubin, G. Hahn, Influence of interference and clamping on fretting fatigue in single rivet-row lap joints, J. Tribol. 123 (4) (2001) 686–698, http://dx.doi.org/10.1115/1.1352746, cited By 45.
[49] H. Taghizadeh, T. Chakherlou, A. Aghdam, Prediction of fatigue life in cold expanded Al-alloy 2024-T3 plates used in double shear lap joints, J. Mech. Sci. Technol. 27 (5) (2013) 1415–1425, http://dx.doi.org/10.1007/s12206-013-0322-5, cited By 19.
[50] T. Chakherlou, B. Abazadeh, J. Vogwell, The effect of bolt clamping force on the fracture strength and the stress intensity factor of a plate containing a fastener hole with edge cracks, Eng. Fail. Anal. 16 (1) (2009) 242–253, http://dx.doi.org/10.1016/j.engfailanal.2008.03.002, cited By 95.
[51] R. Oskouei, An investigation into bolt clamping effects on distribution of stresses and strains near fastener hole and its effect on fatigue life, 2005, cited By 7.
[52] R. Budynas, J. Nisbett, Shigley's mechanical engineering design, 2008, cited By 2110.
[53] T. Chakherlou, B. Abazadeh, Investigating clamping force variations in Al2024-T3 interference fitted bolted joints under static and cyclic loading, Mater. Des. 37 (2012) 128–136, http://dx.doi.org/10.1016/j.matdes.2011.12.037, cited By 33.
[54] F. Sen, M. Pakdil, O. Sayman, S. Benli, Experimental failure analysis of mechanically fastened joints with clearance in composite laminates under preload, Mater. Des. 29 (6) (2008) 1159–1169, http://dx.doi.org/10.1016/j.matdes.2007.05.009, cited By 115.
[55] G. Valtinat, I. Hadrych, H. Huhn, Strengthening of riveted and bolted steel constructions under fatigue loading by preloaded fasteners experimental and theoretical investigations, in: Proceedings of the International Conference on Connections in Steel Structures IV, AISC and ECCS, 2000, pp. 464–473, cited By 23.
[56] H. Zhang, H. Liu, H. Kuai, Stress intensity factor analysis for multiple cracks in orthotropic steel decks rib-to-floorbeam weld details under vehicles loading, Eng. Fail. Anal. 164 (2024) 108705.
[57] A. Aloisio, M.M. Rosso, M. Fragiacomo, R. Alaggio, Fragility estimate of railway bridges due to concrete fatigue, in: Structures, Vol. 49, Elsevier, 2023, pp. 70–87.
[58] T. Endo, M. Matsuishi, On the Fatigue of Metals Under Variable Amplitude Loading, Research report, Kyushu University, Fukuoka, Japan, 1968, Presented at the Japan Society of Mechanical Engineers.
[59] K. Smith, A stress-strain function for the fatigue of metals, J. Mater. 5 (1970) 767–778.
[60] R.I. Stephens, A. Fatemi, R.R. Stephens, H.O. Fuchs, Metal Fatigue in Engineering, John Wiley & Sons, 2000.
[61] F.A. Kandil, M.W. Brown, K. Miller, Biaxial low-cycle fatigue failure of 316 stainless steel at elevated temperatures, in: Mechanical Behaviour and Nuclear Applications of Stainless Steel At Elevated Temperatures, 1982.
[62] M.W. Brown, K. Miller, A theory for fatigue failure under multiaxial stress-strain conditions, Proc. Inst. Mech. Eng. 187 (1) (1973) 745–755.
[63] A. Fatemi, D.F. Socie, A critical plane approach to multiaxial fatigue damage including out-of-phase loading, Fatigue Fract. Eng. Mater. Struct. 11 (3) (1988) 149–165.
[64] O. Basquin, An energy based approach to the simulation of fatigue crack initiation in metal forming tools, in: Proc. ASTM, Vol. 10, 1910, pp. 625–630.
[65] O.H. Basquin, The exponential law of endurance tests, in: Proc Am Soc Test Mater, Vol. 10, 1910, pp. 625–630.
[66] B. Standard, Eurocode 3—Design of steel structures—, BS EN 1 (1) (1993) 2005.
[67] British Standards Institution, BS 5400-10: Steel, Concrete, and Composite Bridges. Code of Practice for Fatigue, British Standards Institution (BSI), London, United Kingdom, 1980.
[68] E. Maiorana, M. Zorzan, et al., Il montaggio e il varo del ponte ferroviario sul Polcevera a Genova, Costruzioni Met. 3 (2011) 32–40.
[69] Norme Tecniche per le Costruzioni, NTC 2018, Ministry of Infrastructure and Transport, Italy, Rome, Italy, 2018, Decree of 17 January 2018, Official Gazette of Italy, No. 42, February 20, 2018.
[70] Eurocode 3: Design of Steel Structures - Part 1-1: General Rules and Rules for Buildings, EN 1993-1-1, European Committee for Standardization (CEN), Brussels, Belgium, 2005, URL https://www.phd.eng.br/wp-content/uploads/2015/12/en.1993.1.1.2005.pdf, EN 1993-1-1:2005.
[71] A. Aloisio, M.M. Rosso, R. Alaggio, Experimental and analytical investigation into the effect of ballasted track on the dynamic response of railway bridges under moving loads, J. Bridge Eng. 27 (10) (2022) 04022085.
[72] L. Fryba, Vibration of Solids and Structures Under Moving Loads, third ed., Thomas Telford Publishing, London, 1996.
[73] A. Aloisio, R. Alaggio, Probabilistic comparative analysis of vehicle–bridge interaction models for predicting bridge response under moving vehicles, J. Eng. Mech. 150 (3) (2024) 04023121.
[74] Y. Su, X. Ye, Y. Ding, ESS-based probabilistic fatigue life assessment of steel bridges: Methodology, numerical simulation and application, Eng. Struct. 253 (2022) 113802.
[75] Z. Zhao, A. Haldar, F.L. Breen Jr., Fatigue-reliability evaluation of steel bridges, J. Struct. Eng. 120 (5) (1994) 1608–1623.
[76] M.M. Szerszen, A.S. Nowak, J.A. Laman, Fatigue reliability of steel bridges, J. Constr. Steel Res. 52 (1) (1999) 83–92.